Evaluation of $Ho_{100-x-y}Er_xCe_y$ magnetic refrigerants using advanced multisample neutron transmission spectroscopy

Hiroaki Mamiya,[1,*] Noriki Terada,[1] Simon Rosenqvist Larsen,[1] Naohito Tsujii,[1]
Kosuke Hiroi,[2] Takenao Shinohara,[2] and Hossein Sepehri-Amin[1]
[1]*National Institute for Materials Science, Tsukuba 305-0047, Japan*
[2]*Japan Atomic Energy Agency, Tokai 319-1195, Japan*

(Received 24 September 2024; accepted 22 January 2025; published 3 March 2025)

Magnetic refrigeration represents an environmentally friendly and promising technology for cooling applications, particularly in hydrogen liquefaction. Recent advancements have demonstrated a highly efficient cooling protocol utilizing small magnetic-field oscillations near metamagnetic transitions, tested using pure holmium metal. This study investigates ternary alloys substituted with erbium and cerium, specifically $Ho_{100-x-y}Er_xCe_y$ ($x < 100$, $y < 21$), to further enhance the performance of the refrigerant. The control of magnetic entropy is largely dependent on identifying variations in spin configurations. However, analyzing these variations in ternary alloys through neutron diffractometry is time intensive. To address this challenge, a multisample neutron transmission spectroscopy technique was developed and applied at beamline 22 RADEN at Japan Proton Accelerator Research Complex (J-PARC). This approach enabled the simultaneous observation of transmission spectra for 25 different alloy compositions at cryogenic temperatures. The spectra revealed that cerium-doped, erbium-rich alloys primarily exhibit ferromagnetic components, yielding a magnetocaloric effect that exceeds that of pure holmium metal under a 5-T magnetic field. In other alloy compositions, the presence of antiferromagnetic ordered states was indicated by satellite Bragg edges in the spectrum. The magnetocaloric effects associated with metamagnetic transitions from these states tend to diminish as the transitions become more frequent or diffuse due to the alloying. The insights gained from this spectroscopic technique contribute to our understanding of the variations in magnetocaloric properties as a result of alloying. Moreover, the successful simultaneous determination of spin configurations across numerous samples highlights the potential of this spectroscopic approach for widespread use in magnetic property evaluation, particularly in the realm of big data-driven research.

DOI: 10.1103/PhysRevResearch.7.013233

I. INTRODUCTION

Liquid hydrogen is poised to become the primary energy carrier; however, the gas compression cycle used for its liquefaction results in significant operational costs. Magnetic refrigeration offers an alternative liquefaction technique, utilizing the entropy change associated with the phase transition from the paramagnetic to the ferromagnetic state, which has been the subject of extensive research [1–3]. Recent studies have shown that magnetic ordering with complex internal spin structures, such as antiferromagnetism, can produce substantial magnetocaloric effects with a carefully designed cooling protocol [4]. A highly efficient cooling protocol has been developed, which involves a small oscillating magnetic field superimposed on a static field at the metamagnetic transition point. This method has proven effective, demonstrating the transition from a helical to a conical spin structure in pure holmium (Ho) metal [5]. These results suggest that various complex spin structures, previously overlooked as magnetic refrigerants, can play significant roles in next-generation magnetic refrigeration technologies. For instance, while pure Ho metal has been effective in demonstrating this protocol, it may not be the optimal refrigerant, as additive elements can alter the magnetic structure to enhance its suitability for magnetic refrigeration applications. Although only 14 rare-earth elements are capable of significantly substituting Ho atoms [6], transition metals such as zirconium can also be doped in small quantities [7]. This opens up a broad range of possibilities for this technology, especially considering alloys related to pure Ho used in initial experiments.

In exploring holmium alloys, research has particularly focused on the ternary alloy system $Ho_{100-x-y}Er_xCe_y$. This direction is supported by prior studies on binary alloys, which have shown that substituting erbium (Er) [8,9] and cerium (Ce) [10,11] can significantly alter the spin structure. In the case of Er, substituting Ho with Er changes the magnetic anisotropy from the easy-plane characteristic of Ho to the easy-axis anisotropy due to a reversal in the Stevens factor. This substitution results in a variety of spin structures in the binary alloy system $Ho_{100-x}Er_x$, including (001) basal-plane helical, tilted helical, cycloidal, *c*-axis longitudinally modulated, and conical configurations, along with a disordered

*Contact author: MAMIYA.Hiroaki@nims.go.jp

phase [9]. Conversely, substituting with lighter rare-earth atoms such as Ce, which has a larger atomic radius, tends to stabilize ferromagnetic structures [10], a change attributed to alterations in the Fermi-surface topology [12,13]. The diverse spin structures in $Ho_{100-x-y}Er_xCe_y$ are expected to exhibit entropy change properties favorable for magnetic refrigeration protocols.

Understanding these spin structures is crucial for managing the magnetic entropy changes associated with magnetic transitions. Conventionally, these structures are determined using neutron diffractometers. While high-intensity neutron beams from nuclear reactors and accelerator facilities can precisely clarify complex spin structures in selected samples, this method is inefficient for quickly assessing spin structures across numerous candidates. The inefficiency stems from the fact that conventional diffractometers can only position one sample at a time at the center of the detector array to measure scattering intensity at each diffraction angle. If the entire process of placing a single sample at the center, cooling it to the boiling point of hydrogen, measuring the diffraction pattern, warming it to room temperature, and then replacing the sample takes half a day, it would require a week of machine time to measure a dozen samples. Given the limited availability of machine time at large facilities, finding an alternative to neutron diffractometry is crucial to efficiently screen the vast array of holmium ternary alloys being investigated as potential magnetic refrigerants.

In the fields of archaeology and metallurgy, neutron transmission spectroscopy has emerged as a viable alternative to neutron diffractometry [14,15]. This technique observes that the intensity of transmitted neutrons decreases at wavelengths corresponding to diffraction events. This phenomenon, known as the Bragg edge, is analyzed in neutron transmission spectra to nondestructively determine crystallographic information within bulky objects [16]. Recent advancements have shown that spin structures can also be evaluated by analyzing magnetic Bragg edges [17,18]. Notably, spectra from parallel beams relate solely to diffractions along each path to the detector, rather than the paths of diffracted neutrons. This configuration allows for the simultaneous measurement of spectra from multiple samples if a position-sensitive detector is installed behind an array of samples exposed to parallel neutron beams. This capability significantly enhances the utility of neutron transmission spectroscopy as a multisample evaluation method, enabling high-throughput assessment of spin configurations at the boiling point of hydrogen.

In this study, a multisample neutron transmission spectroscopy technique was developed and applied to determine the spin structures in 25 samples of the ternary alloy system $Ho_{100-x-y}Er_xCe_y$, utilizing the magnetic Bragg edges in the spectra. The data obtained elucidated the relationship between magnetic entropy changes and the alterations in spin structures resulting from the substitution of Er and Ce. This insight into ternary alloys is invaluable for identifying magnetic refrigerants optimized for hydrogen liquefaction protocols. Furthermore, the effectiveness of multisample neutron transmission spectroscopy has been demonstrated, positioning this method as a robust tool for the high-throughput evaluation of spin configurations in magnetic materials.

II. MULTISAMPLE NEUTRON TRANSMISSION SPECTROSCOPY

Neutron transmission is characterized by an exponential decay represented as $\mathrm{Tr}(\lambda) = e^{-\sum \mu_i(\lambda) t_i}$, where $\mu_i(\lambda)$ and t_i denote the attenuation coefficient and the effective thickness of the i^{th} phase, respectively [19,20]. Typically, $\mu_i(\lambda)$ can be expressed as a sum of contributions from different scattering mechanisms:

$$\mu_i(\lambda) = \mu^{\mathrm{ela}}_{\mathrm{coh},i}(\lambda) + \mu^{\mathrm{ela}}_{\mathrm{incoh},i}(\lambda) + \mu^{\mathrm{inela}}_{i}(\lambda) + \mu^{\mathrm{abs}}_{i}(\lambda),$$

where $\mu^{\mathrm{ela}}_{\mathrm{coh},i}(\lambda)$, $\mu^{\mathrm{ela}}_{\mathrm{incoh},i}(\lambda)$, $\mu^{\mathrm{inela}}_{i}(\lambda)$, and $\mu^{\mathrm{abs}}_{i}(\lambda)$ denote the contributions from coherent elastic scattering, incoherent elastic one, inelastic one, and absorption, respectively. For crystalline phases, $\mu^{\mathrm{ela}}_{\mathrm{coh},i}(\lambda)$ arises primarily from Bragg scattering, which involves the periodic structures of the nucleus and magnetic moments m. In randomly oriented polycrystalline materials, nuclear Bragg scattering occurs at wavelengths λ that are less than twice the lattice interval, $d_{hkl} = 2\pi |\boldsymbol{G}_{hkl}|^{-1}$. This condition gives rise to an edgelike feature in the transmission spectrum, known as the Bragg edge, observed at $2d_{hkl}$ [20]. This characteristic can be modeled using the Heaviside step function H_p. Similarly, the magnetic Bragg edge occurs at $\lambda = 2d_\tau$, where $d_\tau = 2\pi |\boldsymbol{Q}_\tau|^{-1}$ and $\boldsymbol{Q}_\tau$ represents the propagation vector of the spin structure. For unpolarized neutrons, the coherent elastic attenuation coefficient $\mu^{\mathrm{ela}}_{\mathrm{coh},i}(\lambda)$ can be expressed as follows [18,19]:

$$\mu^{\mathrm{ela}}_{\mathrm{coh},i} = \frac{n_N \lambda^2}{2 v_N} \sum_{hkl} d_{hkl} |F_N(\boldsymbol{G}_{hkl})|^2 \cdot H_p(2d_{hkl} - \lambda) + \frac{n_M \lambda^2}{2 v_M} \sum_{\tau} d_\tau |F_M(\boldsymbol{Q}_\tau)|^2 \cdot H_p(2d_\tau - \lambda),$$

where n_{N} and n_{M} represent the total numbers of crystalline and magnetic unit cells per unit volume, respectively; v_{N} and v_{M} are their respective unit-cell volumes and $F_N(\boldsymbol{G}_{hkl})$ and $F_M(\boldsymbol{Q}_\tau)$ denote the crystalline and magnetic structure factors, respectively.

The analysis extends to typical spin structures such as ferromagnet, where the periodicity of the magnetic structure corresponds to the crystalline structure, implying $d_\tau = d_{hkl}$. The height of the magnetic Bragg edge is calculated as $|F_M(\boldsymbol{Q}_\tau)|^2 = \left(\frac{r_m f}{2\mu_B}\right)^2 (m \sin\Theta)^2$, where r_{m} is the magnitude factor (5.39 fm), f denotes the magnetic form factor, and Θ is the angle between $\boldsymbol{m}$ to $\boldsymbol{G}_{hkl}$ [18,19]. Notably, neutrons can be scattered with $m_\perp = m \sin\Theta$, which corresponds to the vector projection of m in the plane perpendicular to the scattering vector, $\boldsymbol{G}_{hkl}$. In cases involving antiferromagnetic modulation $m_\perp \cos(\boldsymbol{Q}_\tau \cdot \boldsymbol{r}_{\mathrm{j}})$ with a single $\boldsymbol{Q}_\tau$, the magnetic structure factor can be further considered as shown below:

$$F_M(\boldsymbol{Q}_\tau) = \sum_j \left(\frac{r_m f}{2\mu_B} m_\perp \cos(\boldsymbol{Q}_\tau \cdot \boldsymbol{r}_j)\right) e^{i\boldsymbol{G}_{hkl}\cdot\boldsymbol{r}_j} = \left(\frac{r_m f}{2\mu_B}\right) \sum_j m_\perp [e^{i(\boldsymbol{G}_{hkl}+\boldsymbol{Q}_\tau)\cdot\boldsymbol{r}_{\mathrm{j}}} + e^{i(\boldsymbol{G}_{hkl}-\boldsymbol{Q}_\tau)\cdot\boldsymbol{r}_j}].$$

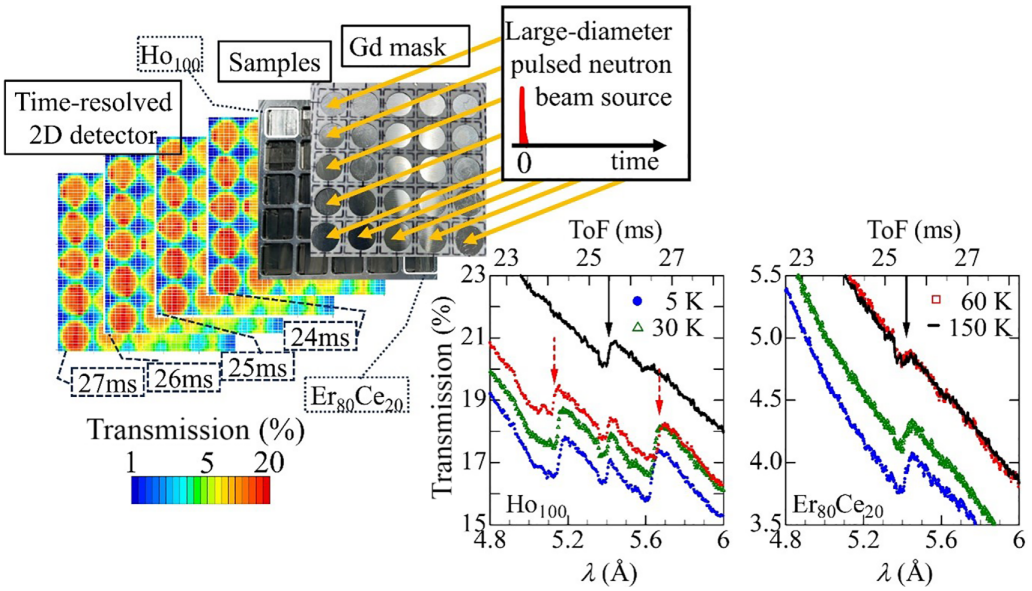

FIG. 1. Schematic diagram of the multisample neutron transmission spectroscopy setup and the obtained time-of-flight (TOF) dependence of neutron transmission for typical compositions, where the wavelength λ is proportional to TOF. The main and satellite Bragg edges, indicated by solid and dashed arrows, originate from the nuclear and ferromagnetic scattering, and long-periodic antiferromagnetic scattering, respectively, and appear at λ corresponding to their period.

The magnetic Bragg edge is affected by the spin structure, splitting into two satellites at $2\pi|\boldsymbol{G}_{hkl} \pm \boldsymbol{Q}_\tau|^{-1}$. For a (001) basal-plane helical antiferromagnetic structure, the edge height $|F_M(\boldsymbol{Q}_\tau)|^2$ is given by $(\frac{r_m f}{2\mu_B} m)^2 (1 + \cos^2\Theta)/4$, where Θ denotes the angle from $\boldsymbol{G}_{hkl}$ to the axis perpendicular to the basal plane.

III. EXPERIMENT

Twenty-five samples of the ternary alloy system $Ho_{100-x-y}Er_xCe_y$ ($0 \leqslant x \leqslant 100$, and $0 \leqslant y \leqslant 21\%$) were synthesized via arc melting of Ho (99.9%), Er (99.9%), and Ce (99.95%) in an argon atmosphere. The resulting button ingots were turned and remelted at least four times to ensure compositional homogeneity. The phase composition of the samples was characterized using x-ray diffractometry with Cu Kα radiation. The AC susceptibility, $\chi' + i\chi''$, was measured under an AC magnetic field $h_{AC}\sin(2\pi ft)$ using a mutual-induction based susceptometer (Quantum Design, PPMS). The amplitude of h_{AC} was set to 0.8 kA/m, and the frequency f varied from 56 to 1778 Hz. Additionally, a static magnetic field ($\mu_0 H_{bias}$) was isothermally superimposed on the AC magnetic field at characteristic temperatures, where μ_0 is the permeability of vacuum. Magnetization M was recorded in magnetic fields ($\mu_0 H$) up to 5 T using a superconducting quantum interference device magnetometer (Quantum Design, MPMS3). The relaxation of the zero-field-cooled magnetization (M_{ZFC}) was measured in $\mu_0 H = 0.01$ T at $T = 50$ K after the alloys had undergone aging in a zero magnetic field for a waiting period t_w at the same temperature. The relaxation rate of M_{ZFC} was calculated as $[(\Delta M_{ZFC})/\Delta(\ln t)]$, where t is the time elapsed after the application of $\mu_0 H$. The field-cooled magnetization M_{FC} was monitored during cooling in $\mu_0 H$ starting from 150 K. The magnetic entropy change (ΔS) was estimated using the Maxwell relation:

$$\Delta S \sim \mu_0 \int_0^H \frac{dM_{FC}}{dT} dH, \tag{1}$$

which remains applicable even for first-order phase transitions with minimal hysteresis [21].

Neutron transmission spectra for the samples were recorded at Beamline 22 (BL22) RADEN at J-PARC MLF [22]. An event-recording-type micropixel chamber-based two-dimensional neutron detector, boron-μNID, featuring a boron-coated neutron converter and an effective detection area of $100 \times 100\,mm^2$, was employed. This detector was positioned 18.6 m from the neutron source. Short-wavelength neutrons ($\lambda < 4$ Å) were filtered out using a disk chopper and a T0 chopper. The neutron beam was shaped into a 50-mm square using a beam collimator, and its flux was reduced to 6 M_{CPS} using the rotary collimator of the RADEN beamline to adjust for the count-rate capabilities of the boron-μNID detector. For the measurements, the beam was split into 25 parallel beams, each with a diameter of 6 mm, using a Gd mask positioned immediately in front of the samples, as shown in Fig. 1. To align with the positions of the split beams, plates from 25 samples, each 2.0 mm thick, were mounted on an aluminum sample holder filled with helium exchange gas for thermal management. Since the shapes of the sample plates did not always correspond precisely to individual beam cells, multiple plates were arranged in a single layer. This assembly was placed in a 4 K cryostat located on the direct beamline between the neutron source and the detector.

Neutron intensities transmitted through the 25 samples were simultaneously measured as a function of time of flight (TOF). Measurements were performed at temperatures of 5, 30, 60, and 150 K, achieving a TOF resolution of approximately 60 μs (≈0.2%) at λ ≈ 5 Å [22]. Each measurement

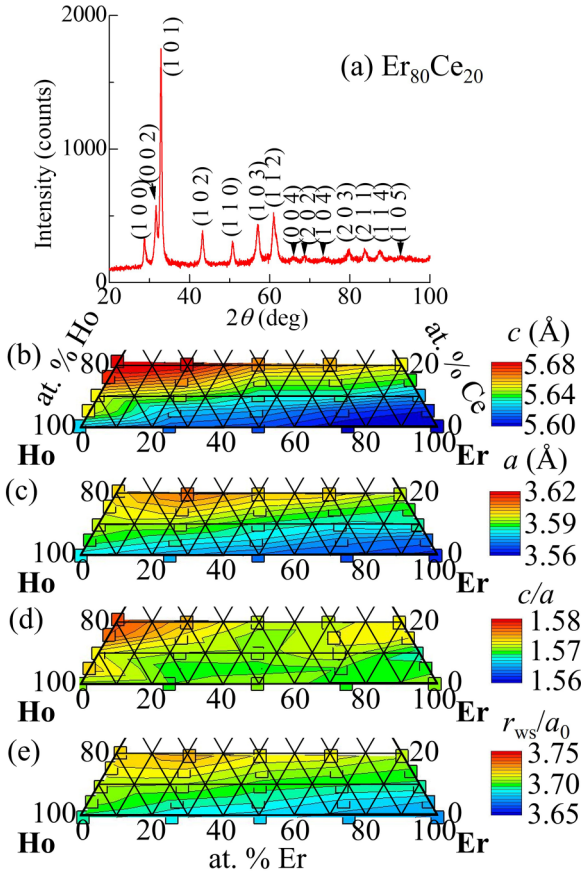

FIG. 2. X-ray-diffraction (XRD) pattern of a typical composition of $Er_{80}Ce_{20}$ (a) and compositional dependence of the hexagonal close-packed structure, determined from XRD patterns. Lattice constants *a, c*, and their axial ratio *c/a* are plotted on the ternary-state diagram in panels (b)–(d). The estimated Wigner-Seitz radii (r_{WS}) are expressed in units of the Bohr radius (a_0) in panels (e).

session lasted 10 h to ensure that the minimum signal amplitude in each bin with the time width of 100 μs exceeded 100 000 counts, even for erbium-rich alloys, which are known for their strong neutron absorption. Future improvements in neutron-beam flux and detector count-rate capabilities are expected to significantly reduce measurement times.

IV. RESULTS AND DISCUSSION

A. Crystalline structure

Figure 2(a) presents the x-ray-diffraction (XRD) pattern of a typical $Er_{80}Ce_{20}$ composition. (For XRD patterns of other samples, see Ref. [23].) The observed peaks correspond to diffractions from a hexagonal close-packed (hcp) structure ($P6_3/mmc$). No impurity peaks were detected, confirming that all alloys are single phased. The estimated lattice constants exhibited a decrease with increasing Er content and an increase with Ce content, as depicted in Fig. 2. For theoretical comparisons [12], the Wigner-Seitz radius (r_{WS}) and the axial ratio (*c/a*) were calculated. As shown in Fig. 2(e), r_{WS} decreases with increasing Er concentration, consistent with the expected difference of $0.01a_0$ in r_{WS} between Ho and Er, where a_0 represents the Bohr radius (52.9 pm). Conversely, the variation in r_{WS} with Ce substitution was slightly larger than anticipated for doping with Ce, which has an r_{WS} of $3.81a_0$. This pattern aligns with previous studies of binary alloys $Ho_{100-y}Ce_y$ and $Er_{100-y}Ce_y$ [24,25]. Figure 2(d) demonstrates that the axial ratio (*c/a*) increases significantly with Ce substitution in Ho-rich alloys, whereas the change in *c/a* for Er-rich alloys is minimal in comparison. These trends are consistent with earlier reports [24,25]. Comparing these observations with theoretical predictions, which suggest that ferromagnetism is stabilized in rare-earth alloys with larger *c/a* ratios and less-contracted lattices [12], it appears that Ce-doped Ho-rich alloys most closely satisfy these conditions.

B. Magnetic entropy change

Let us now examine the magnetocaloric effects of the ternary alloys. The magnetic entropy changes (ΔS) induced by applying a magnetic field $\mu_0 H$ at a given temperature T are depicted as contour maps in Fig. 3. These maps were generated by calculating ΔS using the Maxwell relation for $M_{FC}(H, T)$. The contour maps typically exhibit complex landscapes, characterized by multiple valleys (indicated in red color) and ridges (indicated in purple color), with the deepest and highest points in each region marked by diamonds (◊) and crosses (×), respectively. (No markings are provided when the highest point occurs at zero magnetic field.) Figure 4(a) illustrates typical cross sections of the valleys for the alloys in the leftmost column, highlighting that the valleys deepen with increasing magnetic-field strength. This trend is consistent across all valleys in the ΔS landscapes shown in Fig. 3. This phenomenon suggests that the application of a magnetic field promotes uniform alignment of magnetic moments along the field direction, transitioning the system from less-ordered states and thereby decreasing magnetic entropy. Conventionally, these less-ordered states are considered paramagnetically fluctuating. However, certain alloys show two distinct troughs, observed prominently in the red-framed panels, corresponding to the Ce-doped Ho-rich alloy group. The nature of the less-ordered state at zero magnetic field on the low-temperature side of these valleys remains unclear. Addressing this ambiguity is crucial for a comprehensive understanding of the magnetocaloric effects in ternary alloy systems.

Next, we explore the formation of ridges in the magnetic entropy landscape, which indicates an increase in magnetic entropy with increasing magnetic-field strength—a phenomenon referred to as the inverse magnetocaloric effect. As shown in Fig. 3, the configuration and characteristics of these ridges differ significantly across alloys of different compositions, leading to the identification of four distinct ridge types based on the locations of the highest points (×). The first ridge type is observed in alloys with compositions similar to pure Ho and pure Er, where the highest points are located on the high-temperature, high-field side of the ridges. A representative cross section for the $Ho_{75}Er_{25}$ alloy is presented in Fig. 4(b). It is well established that pure Ho and pure Er exhibit paramagnetic-to-antiferromagnetic transitions at higher temperatures. The observed inverse magnetocaloric effects emerge when antiferromagnetic order is destabilized by the application of a magnetic field. Therefore, the ridges observed in alloys resembling the compositions of pure Ho

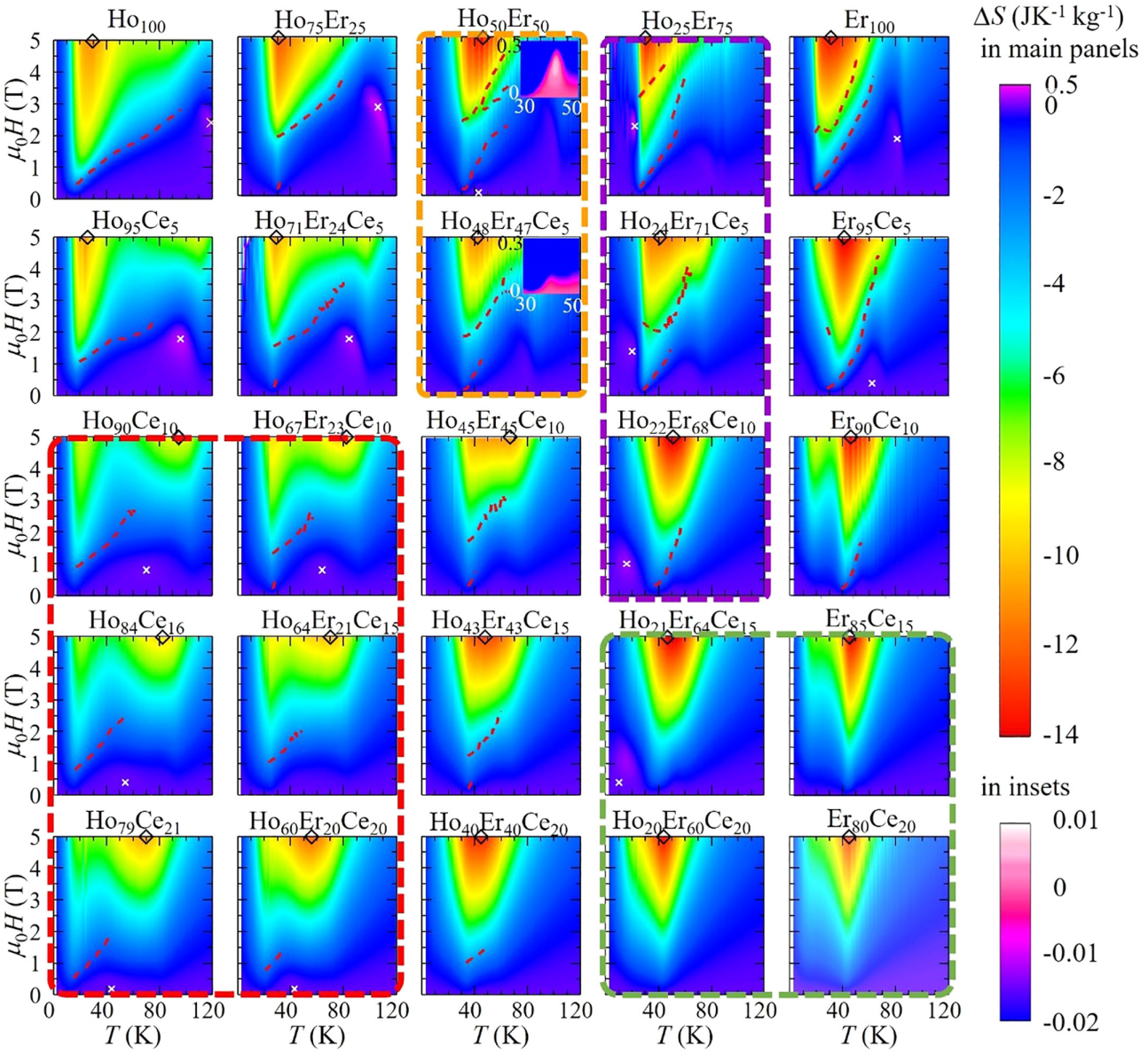

FIG. 3. Contour maps of the magnetic entropy changes (ΔS) induced by applying a magnetic field $\mu_0 H$ at temperature T. Symbols ($\Diamond$) and ($\times$) denote conditions where ΔS reaches its minimum and maximum, respectively. Red broken curves on the contour maps indicate the magnetic fields (H_m) where the variation rate $[(\Delta S/\Delta)(\mu_0 H)]$ peaks. These correspond to the deepest points in the valleys, the highest points at the ridges, and the locations of the scarps in the ΔS landscapes, respectively. Colored frames categorize groups based on landscape features. The insets are enlarged views of the low-field region.

and pure Er at higher temperatures can be attributed to this mechanism.

Setting aside the well-established behavior of pure Ho and Er metals, a second type of ridge is observed in the Ce-doped Ho-rich alloy group, where the highest point lies in the middle of a gentle ridge. A representative cross section for the $Ho_{85}Ce_{15}$ alloy at $T = 54$ K is depicted in Fig. 4(a). The third type is a minor ridge in the low-field region, exemplified by the $Ho_{50}Er_{50}$ alloy in Fig. 4(b) (see also insets in Fig. 3). A similar anomaly observed in the $Ho_{48}Er_{47}Ce_5$ alloy at $T =$ 40 K suggests that this type of ridge is characteristic of the $Ho_{50}Er_{50}$ base alloy group, outlined in orange frames. The fourth ridge type emerges at very low temperatures, approximately 20 K, as observed in the $Ho_{25}Er_{75}$ alloy in Fig. 4(b). These ridges are characteristic of the $Ho_{25}Er_{75}$ base alloy group, highlighted in purple-framed panels. As described, the latter three ridge types exhibit distinct features that differ from those of pure Ho and Er, raising uncertainty as to whether they are associated with similar antiferromagnetic behaviors. This represents the second major issue requiring resolution.

Finally, it is important to note that the presence of a scarp is generally observed between valleys and ridges, characterized by a steep gradient (indicated by red dashed lines within each panel of Fig. 3). For instance, in pure Ho metal, as shown in Fig. 4(a), ΔS decreases gradually as the magnetic field H increases from zero. The rate of decrease accelerates sharply around $\mu_0 H_m = 0.5$ T, before moderating at higher fields. The magnitude of $\mu_0 H_m$ increases with 5% Ce doping

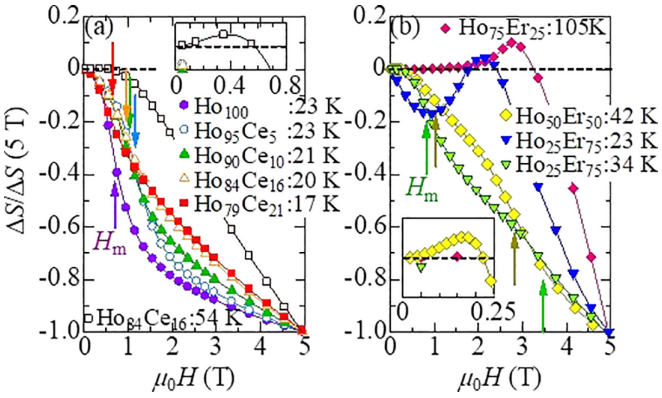

FIG. 4. Typical cross-sectional views of the ΔS landscapes from Fig. 3. (a) Cross sections of alloys in the leftmost column of Fig. 3 at temperatures where $[(\Delta S/\Delta)(\mu_0 H)]$ is maximized (and at the temperature where ΔS for $Ho_{85}Ce_{15}$ is positive and maximal); (b) Cross sections of alloys in the top row of Fig. 3 at temperatures where ΔS reaches a maximum (sections containing ridge peak points), and at temperatures highlighting the multistage structure for $Ho_{25}Er_{75}$. The arrows indicate the magnetic fields H_m where the decreasing rates are maximal.

but decreases with further Ce substitution in the Ce-doped Ho-rich alloy group. Conversely, for $Ho_{50}Er_{50}$ and $Ho_{75}Er_{25}$ alloys, ΔS exhibits two distinct magnetic-field ranges where sharp decreases occur. These multistep structures are characteristic of the $Ho_{50}Er_{50}$ and $Ho_{25}Er_{75}$ base alloy groups, as shown by multiple dashed lines in each panel. In contrast, the Ce-doped Er-rich alloy group, marked by green-bordered panels, displays a monotonous variation in ΔS without scarp formations in the landscape. The third major issue to address is to clarify the reason some alloys exhibit scarp formations while others do not. In summary, beyond the well-documented cases of pure Ho and Er metals, it is essential to understand the origins of characteristic structures such as twin valleys, various types of ridges, and the presence or absence of scarps observed in the ΔS landscapes across different concentration ranges. To this end, we begin by examining the macroscopic magnetic responses to uncover the underlying mechanisms.

C. Macroscopic magnetic properties

Figure 5 illustrates the temperature dependence of field-cooled magnetization (M_{FC}) for typical alloys in magnetic fields of $\mu_0 H$ values 0.01, 1.0, 4.2, and 5.0 T (data for all alloys at these fields can be found in Ref. [23]). In Fig. 5(a), χ_{FC} at 0.01 T increases as the temperature decreases from 150 K. This temperature dependence can be described by the formula $\frac{n\mu_0 m_{eff}^2}{3k_B(T-T_w)}H$ until cusps or broad humps manifest at a specific temperature T_{c1} on $M_{FC}(T)$. Here, n represents the atomic density, m_{eff} is the effective magnetic moment, k_B is the Boltzmann constant, and T_w is the Weiss temperature (equivalent to the paramagnetic Curie temperature), indicating the mean amplitude of magnetic interactions. Both m_{eff} and T_w decrease with substitution, as depicted in Figs. 6(a) and 6(c). The trend in m_{eff} parallels that of the saturation magnetization M_s when M_{FC} (5 T, 2 K) is considered as M_s, given the minor difference between M_{FC} (4.2 T, 2 K) and M_{FC} (5 T, 2 K), as shown in

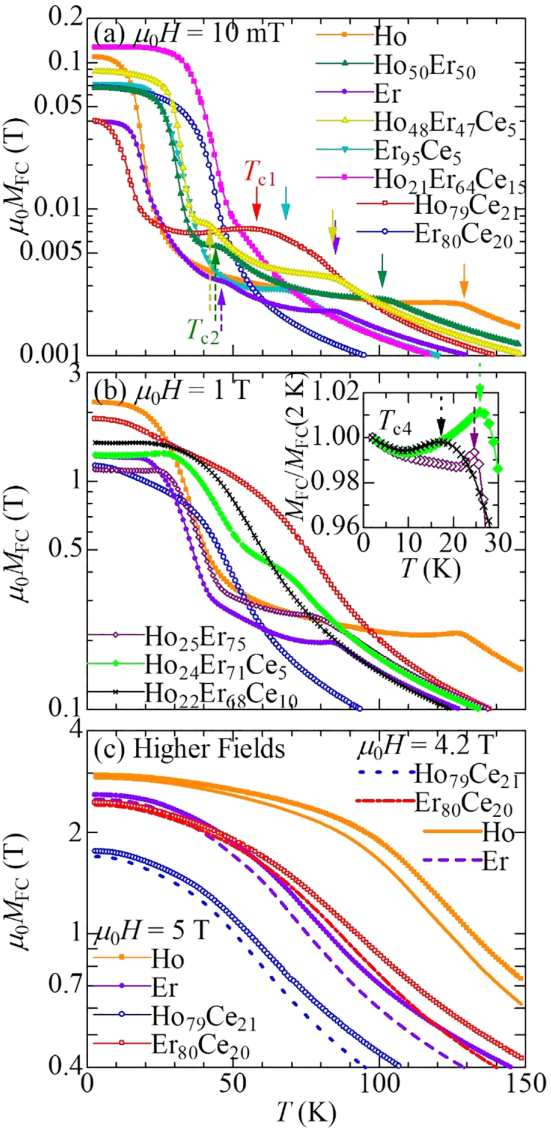

FIG. 5. Temperature dependence of field-cooled magnetization (M_{FC}) for typical alloys in magnetic fields $\mu_0 H$ of 0.01, 1.0, 4.2, and 5.0 T. Solid, dashed, and dotted arrows mark the characteristic temperatures T_{c1}, T_{c2}, and T_{c4} at which $M_{FC}(T)$ exhibits a cusp or broad hump, respectively. The inset provides an enlarged view of the low-temperature range, displaying M_{FC} normalized by its magnitude at 2 K for ease of comparison.

Fig. 5(c). The observed m_{eff} can be explained by the average value of $\sqrt{\langle m_{calc}^2 \rangle}$ calculated for isolated rare-earth ions with total angular momentum J, where m_{calc} is $g\sqrt{J\,(J\,+\,1)}$ and g is the Landé g factor [refer to Fig. 7(b)]. Conversely, the observed variation in T_w aligns with the average value of de Gennes's factor $G = (g-1)^2\,J\,(J\,+\,1)$, as conventionally expected for rare-earth alloys [26] [see Fig. 7(a)]. These observations suggest that the magnetic properties above T_{c1} can be interpreted as a paramagnetic state with ferromagnetic interactions on average.

Figure 6(d) presents the composition dependence of T_{c1} [regions where no cusps or humps were detected on $M_{FC}(T)$ are left blank]. It was observed that T_{c1} decreased alongside

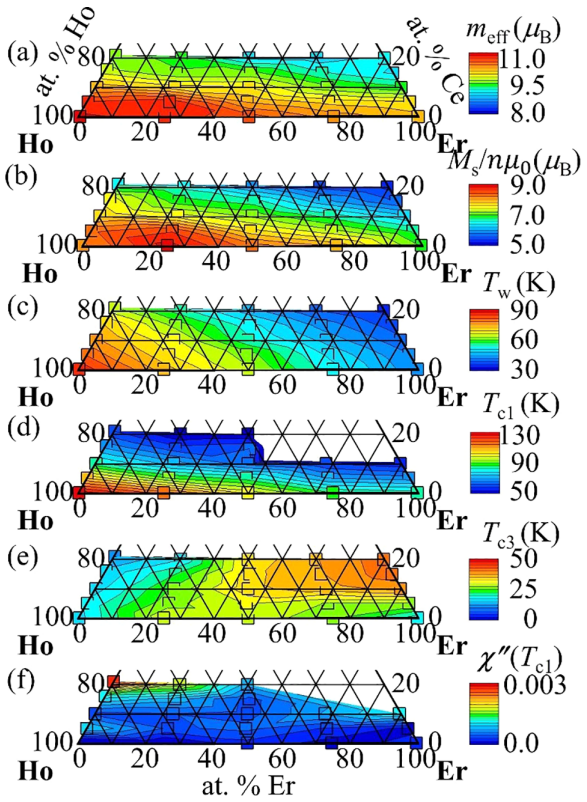

FIG. 6. Compositional dependence of (a) effective magnetic moment m_{eff}, (b) saturation magnetization $M_s/n\mu_0$, (c) Weiss temperature T_w, (d) the characteristic temperature T_{c1} at which $M_{FC}(T)$ shows a cusp or broad hump, and (e) the characteristic temperature T_{c3} at which the gradient of $M_{FC}(T)$ becomes maximum, (f) out-of-phase components of AC susceptibility χ'' at T_{c1}, presented on the ternary-state diagram. Blank areas indicate compositions where no cusp or broad hump were distinguished in $M_{FC}(T)$. Values of *Ms* are normalized by atomic density *n* to facilitate comparison with other measurements.

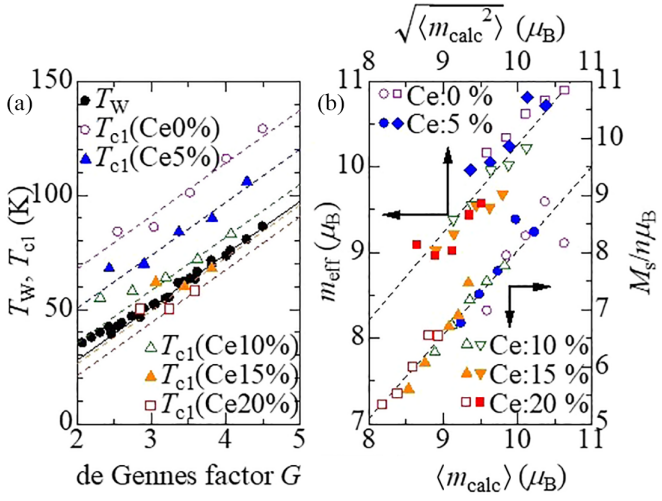

FIG. 7. Scaling relationships shown for (a) Weiss temperature T_w and the characteristic temperature T_{c1} as a function of de Gennes's factor *G*, and (b) effective magnetic moment m_{eff} and saturation magnetization $M_s/n\mu_0$ as a function of the mean value (bottom axis) or root-mean-square (top axis) of the magnetic moment m_{calc} calculated for isolated rare-earth ions.

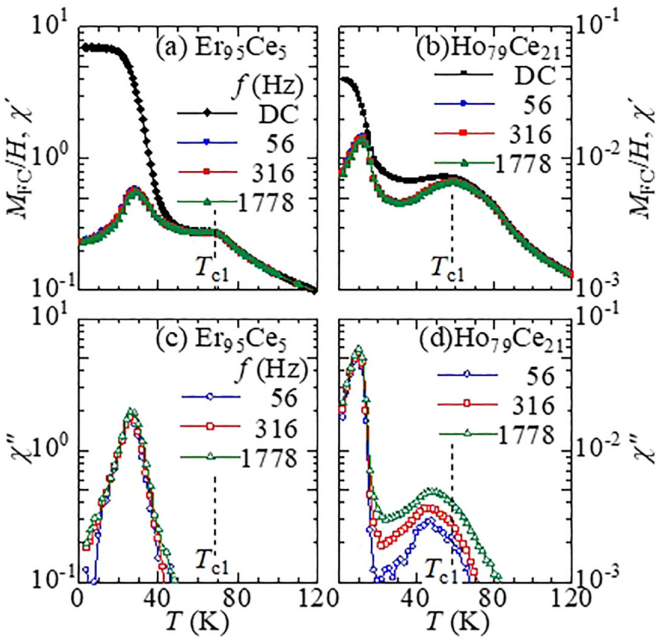

FIG. 8. Temperature dependencies for the in-phase and out-of-phase components of AC susceptibility $\chi' + i\chi''$ with M_{FC}/H for the typical alloys $Ho_{79}Ce_{21}$ and $Er_{95}Ce_5$.

T_w as a result of substitution. Figure 7(a) depicts T_{c1} as a function of *G*. For alloys with constant Ce concentrations, T_{c1} can be scaled by *G* with a gradient similar to that of T_w, while the variations in T_{c1} due to Ce substitution are steeper than those in T_w. This pattern is consistent with previously reported behaviors of light rare-earth doped–heavy rare-earth binary alloys [11]. Conventionally, a cusp or hump in $M_{FC}(T)$ for heavy rare-earth based alloys has been associated with antiferromagnetic ordering of magnetic moments [11]. However, the dynamic properties discussed below suggest that antiferromagnetism may not necessarily be the origin of the cusp/hump at T_{c1} in certain alloys.

Figure 8 presents the typical temperature dependencies of the in-phase and out-of-phase components of AC susceptibility $\chi' + i\chi''$ alongside M_{FC}/H for $Ho_{79}Ce_{21}$ and $Er_{95}Ce_5$ (data for all alloys are provided in Ref. [23]). Near T_{c1}, χ'' exhibited frequency-dependent peaks for $Ho_{79}Ce_{21}$, while such peaks were negligible for $Er_{95}Ce_5$ in the temperature range just below T_{c1}. Notably, significant χ'' values below T_{c1} are observed only in the Ce-doped Ho-rich alloy group, as shown in Fig. 6(f). The relaxation rate of zero-field-cooled magnetization M_{ZFC}, $[(dM_{ZFC})/d(\ln t)]$ for $Ho_{79}Ce_{21}$ and $Er_{95}Ce_5$ are shown in Fig. 9. At 50 K ($<T_{c1}$), $[(dM_{ZFC})/d(\ln t)]$ for $Ho_{79}Ce_{21}$ peaked when the elapsed time *t* matched the waiting period t_w before magnetic-field application. This behavior suggests that the spin configuration slowly stabilized during t_w, and as a result, departing from a deeper free-energy minimum requires a longer response time. In contrast, such behavior was not observed for $Er_{95}Ce_5$, as shown in Fig. 9(a). The frequency-dependent peak of χ'' and the t_w-dependent relaxation are established characteristics of spin glasses [27]. Based on this, we cannot disregard the possibility that the peaks in $M_{FC}(T)$ for the Ce-doped Ho-rich alloy

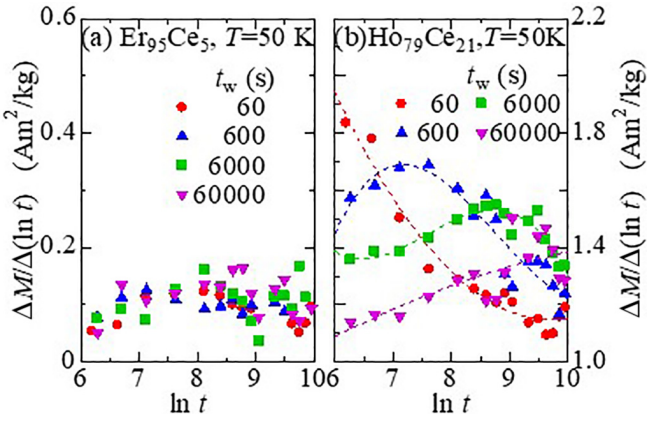

FIG. 9. Relaxation rate of M_{ZFC}, $[(\Delta M_{\mathrm{ZFC}}/\Delta)(\ln t)]$, for the typical alloys $Ho_{79}Ce_{21}$ and $Er_{95}Ce_5$, measured after the application of $\mu_0 H$ of 0.01 T at $T = 50$ K, where the alloys were aged for a waiting time t_w in zero magnetic field at the same temperature before the application of H.

group originate from spin-glass ordering, whereas the peaks for the Er-rich alloy group are likely associated with the onset of antiferromagnetic ordering. Therefore, in addressing the first issue, both antiferromagnetism and spin glass must be considered as potential candidates for the less-ordered states observed at lower temperatures.

In the discussion of the cusp/hump observed in $M_{\mathrm{FC}}(T)$, it is important to note that secondary humps manifest near T_{c2} when $Ho_{50}Er_{50}$ and $Ho_{48}Er_{47}Ce_5$ are cooled further from T_{c1} at $\mu_0 H$ of 0.01 T [see dashed arrows in Fig. 5(a)]. Recently, Cowley *et al.* investigated the presence of a new type of disordered phase in this temperature range for the $Ho_{57}Er_{43}$ alloy [9]. It would be interesting to determine whether such a novel phase is associated with the low-field ridge identified in the contour map for the $Ho_{50}Er_{50}$ base alloy group. The phenomena occurring at T_{c1} and T_{c2} will be revisited in the discussion of neutron transmission spectra, as macroscopic measurements alone are insufficient to definitively distinguish between spin-glass or novel-disordered phases and antiferromagnetic-ordered states.

Next, we shift our focus to the lower-temperature range, where all $M_{\mathrm{FC}}(T)$ measurements at $\mu_0 H$ of 0.01 T show a significant increase as the temperature decreases. The characteristic temperature at which the gradient of $M_{\mathrm{FC}}(T)$ reaches its maximum, designated as T_{c3}, is shown for various compositions in Fig. 6(e). The analysis reveals that T_{c3} of $Ho_{100-x}Er_x$ (Ce: 0%) peaks at $x \sim 50\%$. In the Er-rich region, T_{c3} rises with the substitution of Er by Ce, whereas in the Ho-rich region, T_{c3} declines with Ce substitution. The compositional dependence of T_{c3} does not follow the scaling behavior of G observed for T_w. This trend is consistent with prior reports on the binary alloys $Ho_{100-y}Ce_y$, and $Er_{100-y}Ce_y$ [11]. Typically, the pronounced increase in $M_{\mathrm{FC}}(T)$ signifies the onset of ferromagnetic ordering. However, it remains uncertain whether all such increases in $M_{\mathrm{FC}}(T)$ stem from conventional ferromagnetism. For the $Ho_{25}Er_{75}$ base alloy group, χ_{FC} at 1 T decreases as the temperature drops further from T_{c4} below T_{c3}, as depicted in the inset of Fig. 5(b). This reduction in M_{FC} is atypical for conventional ferromagnets, which typically exhibit a monotonous increase in M_{FC} as spontaneous magnetization grows. Standard references note that M_{FC} decreases with decreasing temperature during spin reorientation transitions [28] or upon reentering spin-glass states [29]. Consequently, a second question arises: does the low-temperature inverse magnetocaloric effect observed in the $Ho_{25}Er_{75}$ base alloy group result from a reorientation of ordered magnetic moments, or does it stem from a disruption of the magnetic order itself? Addressing this question requires microscopic information. Thus, we turn our attention to the neutron transmission spectra.

D. Neutron transmission spectra

Since the origins of the observed characteristic magnetocaloric effects cannot be definitively determined from macroscopic measurements alone, the neutron transmission spectra of the 25 ternary alloys were examined simultaneously. For the same sample, some variation in the transmission was observed across individual pixels. This variability may be attributed to the narrow gaps between the sample pieces arranged on a single sheet. To reduce this effect, the transmission was averaged over the pixels within the same sample cell. The insets in Fig. 1 display the attenuation spectra $\mu(\lambda)$ of unpolarized neutrons for representative compositions Ho_{100} and $Er_{80}Ce_{20}$ (the spectra for all alloys are detailed in Ref. [23]). Notably, each spectrum at $T = 150$ K exhibits a sawtooth-shaped structure. The positions of these features, indicated by solid arrows, correspond to twice the lattice interval d_{101} of the {101} planes in the unit cell, as determined by x-ray diffraction. These features are identified as {101} Bragg edges, attributed to nuclear scattering, consistent with the paramagnetic state of the alloys at $T = 150$ K.

At temperatures $T = 5$, 30, and 60 K, two additional edges appear in $\mu(\lambda)$ for Ho_{100} (see the dashed arrows in the insets of Fig. 1). These edges, positioned symmetrically on either side of the original {101} Bragg edge, are identified as satellite edges resulting from magnetic scattering by antiferromagnetic structures with longer periodicity $\boldsymbol{Q}_\tau$. This phenomenon is observed in all alloys that display a cusp or hump in $M_{\mathrm{FC}}(T)$ at temperatures below approximately $0.8\,T_{c1}$. Consequently, it is reasonable to attribute the peaks or humps in $M_{\mathrm{FC}}(T)$ at T_{c1} to the initiation of long-range antiferromagnetic periodic ordering, even though we could not confirm the precise emergence of satellite edges at T_{c1}. This limitation arises from the difficulty of analyzing edges smaller than $3\,\mu_{\mathrm{B}}$, given the constraints of the signal-to-noise ratio with the current uniform measurement time. Such limitations are an inherent challenge of multisample transmission spectroscopy, as it is not possible to adjust the measurement time for each sample.

Figure 10(b) illustrates the compositional dependence of these satellite-edge heights m_{AF} normalized by the factor $(\frac{r_m f}{2\mu_B})\sqrt{\frac{n_M \lambda^2 d_{101}}{2v_M}\,\frac{1+\cos^2\Theta_{101}}{4}}$, as described previously, where Θ_{101} is the angle from $\boldsymbol{G}_{101}$ to the ⟨001⟩ axis. Blank areas in the figure correspond to compositions where no satellite edges are discernible. For basal-plane helical antiferromagnets, m_{AF} equals the magnitude of the magnetic moment m in the basal plane. However, for general helical antiferromagnets, m_{AF}

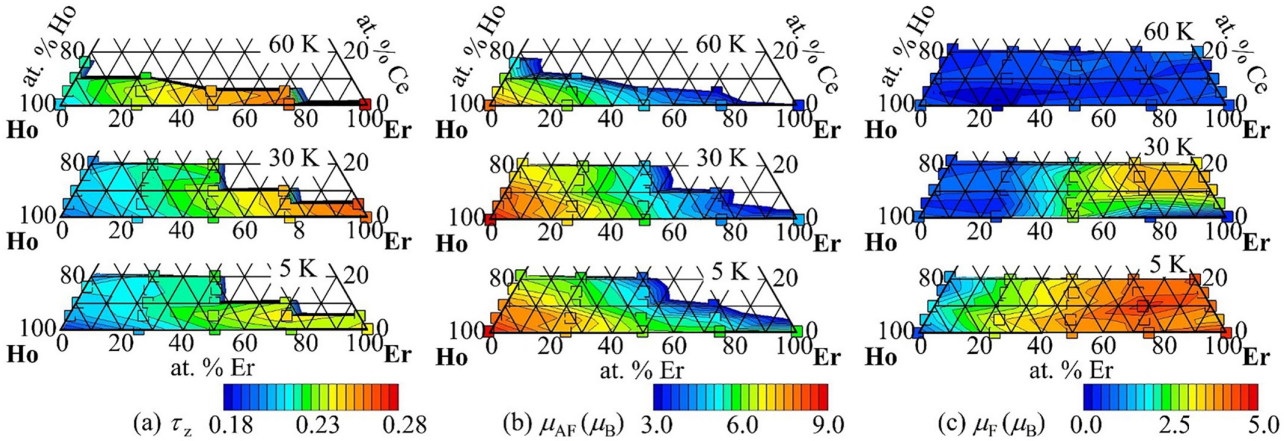

FIG. 10. Compositional dependence of characteristics in neutron transmission spectra at various temperatures. (a) Propagation vector length τ_z estimated from intervals between satellite edges, (b) magnitude of the antiferromagnetic component m_{AF} estimated from satellite edge heights, and (c) magnitude of the ferromagnetic component m_F estimated from the main edge height.

deviates from m due to the difference in the vector projection of $\boldsymbol{m}$ onto the plane perpendicular to $\boldsymbol{G}_{hkl}$. Thus, it is not feasible to determine whether the observed decrease in m_{AF} with substitution arises from a reduction in the length of the ordered $\boldsymbol{m}$ or from the tilting of $\boldsymbol{m}$ from the basal plane. This uncertainty must be accepted in this study, as data from a single set of edges are insufficient to ascertain the orientation of $\boldsymbol{m}$. In the case of Ho_{100}, the estimated value of m_{AF}, 8.9 μ_B at 5 K, closely aligns with the previously reported value for the basal-plane component, 9.7 μ_B at 4 K, in single crystals of Ho [8]. In the Ce-doped Ho-rich alloy group, the estimated m_{AF} values at 5 K are comparable with $M_s/n\mu_0$ as shown in Fig. 6(b). Conversely, the estimated m_{AF} values for other alloys with higher concentrations of Er at 5 K are significantly smaller than $M_s/n\mu_0$. This discrepancy will be discussed later in relation to the presence or absence of coexisting ferromagnetic components.

Figure 10(a) illustrates the compositional dependence of τ_z, $(c/2\pi)\boldsymbol{Q}_\tau = (0,\ 0,\ \tau_z)$, estimated from the intervals of the satellite edges under the assumption that $\boldsymbol{Q}_\tau$ is parallel to the c-axis, as typically observed in heavy rare-earth metals [26]. This suggests that the antiferromagnetic periodicity below T_{c1} is incommensurate in ternary alloys, similar to what is observed in binary alloys [8–11]. It is observed that the period τ_z^{-1} shortens as Ho is replaced by Er, while changes due to Ce doping are minimal. Across all compositions, the periods lengthen as the temperature decreases. These results are largely consistent with extrapolations from trends observed in binary alloys [8–11].

The insights provided by neutron transmission spectroscopy address the first issue: the less-ordered states at low temperatures in the Ce-doped Ho-rich alloy group are not typical spin-glass states devoid of periodic spin order. Instead, they represent antiferromagnetic spin states with incommensurate periodicity. The spin-glass-like dynamic properties observed in these states can be attributed to a form of cluster-glass behavior, characterized by medium-range correlations among clusters with an antiferromagnetic internal structure. This medium-range correlation is probably related to the second type of ridge, where the highest point ($\times$) in the contour maps of ΔS (see Fig. 3) occurs at a much lower temperature than T_{c1} in the Ce-doped Ho-rich alloy group. In other words, the conditions for the maximum inverse magnetocaloric effect in these states differ from those in pure holmium and erbium. However, given the 0.2% resolution of the current spectrum, detailing variations in medium-range correlations based on the width of the Bragg edge is challenging. Unlike microscale ordering, medium-range correlations have little effect on entropy, leaving this aspect unresolved. In conclusion, the observed twin valley structures can be attributed to the higher magnetic entropy in both paramagnetic and antiferromagnetic states compared to that in the uniformly aligned state under a high magnetic field.

Before concluding the discussion on satellite edges, it is important to note the minor phase characterized by the hump observed in the $Ho_{50}Er_{50}$ base alloy group at T_{c2}. In the spectra for $Ho_{50}Er_{50}$, m_{AF} increases from 4.6 μ_B at 60 K to 6.0 μ_B at 30 K. Unfortunately, this temperature interval is too broad to conclusively determine whether a disordered phase exists between $T_{c3} = 29$ K and $T_{c2} = 46$ K. This limitation highlights a significant drawback of multisample neutron transmission spectroscopy, where all samples must be measured at the same preset temperatures.

Shifting focus to the spectrum without satellite edges for $Er_{80}Ce_{20}$, as shown in the inset of Fig. 1, it is notable that the height of the original edge at $\lambda = 2d_{101}$ significantly increases with decreasing temperature from 60 to 5 K. The nuclear scattering intensity for heavy rare-earth metals is expected to remain approximately constant at cryogenic temperatures below their Debye temperatures, even when accounting for the Debye-Waller factor [30]. Therefore, the observed variation in edge height can be attributed to the growth of ferromagnetic components. Figure 10(c) illustrates the compositional dependence of these height increments m_F normalized by the factor $(\frac{r_m f}{2\mu_B})\sqrt{\frac{n_M \lambda^2 d_{101}}{2v_M}(m \sin\Theta_{101})^2}$, where Θ_{101} is the angle from G_{101} to the $\langle 001\rangle$ axis. In c-axis ferromagnets, m_F represents the magnitude of the magnetic moment m along the c-axis. However, as previously noted, the direction of $\boldsymbol{m}$ cannot be determined solely from a single edge. Therefore, the plotted m_F can deviate from $\boldsymbol{m}$ due to the difference in the vector projection of $\boldsymbol{m}$ onto the plane perpendicular

to $\boldsymbol{G}_{101}$ for general ferromagnets with tilted easy axes. The estimated magnitude of m_F for $Er_{80}Ce_{20}$, 4.3 μ_B at 5 K, was smaller than the previously reported value of 6.2 μ_B for the *c*-axis component in single crystals of $Er_{80}Ce_{20}$ [31]. This discrepancy warrants further discussion, particularly because $Er_{80}Ce_{20}$ is known as a *c*-axis ferromagnet. One potential explanation for this discrepancy is the extinction effect due to multiple scattering [20], which was not considered in this analysis. The extinction effect becomes significant when ferromagnetic correlations grow to micrometer scales, as is often the case for ferromagnetic domains. For the strongest (101) reflection, particularly at a long neutron wavelength of 5.4 Å, such effects cannot be ignored [20]. However, the current data from a single edge are insufficient to evaluate the exact magnitude of m_F; therefore, we focus instead on comparing the relative magnitudes of m_F across various compositions and temperatures.

From Fig. 10(c), it is evident that m_F becomes significant as the temperature drops below T_{c3} for all ternary alloys. This observation supports the conclusion that T_{c3} likely marks the onset of the ferromagnetic component. Regarding compositional dependence, the values of m_F for Ce-doped Ho-rich alloys are relatively lower than those for other alloys at 5 K. This suggests that the tilt angles of the magnetic moments from the basal plane in the conical spin structures of the Ce-doped Ho-rich alloy group are relatively small, consistent with earlier findings for pure Ho metal [8]. Conversely, m_F increases with the substitution of Ho by Er, as shown in Fig. 10(c). This increase is attributed to changes in the tilt angle of the cone within the conical spin structures, consistent with discussions of pure Ho and Er metals [8]. For the $Ho_{25}Er_{75}$ base alloy group, m_F at 5 K exceeds its value at 30 K, indicating that ferromagnetic ordering persists at lower temperatures. This finding conclusively resolves the earlier question concerning the additional ridges observed at lower temperatures. Specifically, the inverse magnetocaloric effect observed in this group at T_{c4} ($<T_{c3}$) is not due to a reentrant spin-glass transition. Instead, it must be attributed to spin reorientation transitions. However, the current temperature intervals and signal-to-noise ratios of the spectral data are insufficient to fully analyze the rotations of the ferromagnetic components.

Focusing on the Ce-doped Er-rich alloy group, the magnitude of m_F is substantial enough to draw comparisons with pure Er metal, while satellite edges are absent from their spectra. These findings suggest that alloys in this group behave as simple ferromagnets. The emergence of ferromagnetism in this group, characterized by larger *c/a* ratios and elongated lattice parameters compared to pure Er metal, is consistent with prior theoretical predictions [12]. However, given that a basal-plane helical structure is retained in the Ce-doped Ho-rich alloy group—despite even larger *c/a* ratios and lattice constants—it is likely that magnetic anisotropy plays a crucial role in the stabilization of ferromagnetism. This complex relationship warrants further investigation. At this stage, let us turn our attention to the relevance of the ΔS landscape and the presence or absence of antiferromagnetic components. A comparison of Fig. 10(b) with Fig. 3 reveals that alloys lacking antiferromagnetic components do not exhibit scarp structures in their ΔS landscapes. To further explore this connection, the magnetization curves will be examined in the next subsection.

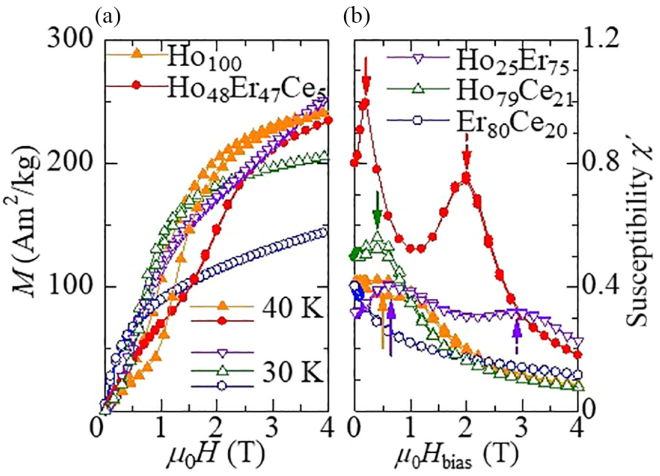

FIG. 11. Responses to the application of a magnetic field for typical alloys. (a) Magnetization curves, and (b) in-phase component χ' of AC susceptibility in the static magnetic- field H_{bias}. Solid and dashed arrows indicate the characteristic fields H_{c1} and H_{c2} at which $\chi'(H_{bias})$ exhibits peaks.

E. Magnetic-field response

Figure 11(a) displays the magnetization curves for typical alloys (complete curves for all alloys are available in Ref. [23]). For pure Ho metal, magnetization (M) increases gradually with an increasing magnetic field (H) from zero at temperatures between T_{c3} and T_{c1} (40 K). At approximately 1 T, the increase in M accelerates abruptly, followed by a return to a more gradual increase as H continues to rise. This single, stepwise increase in M has been attributed to a metamagnetic transition from an antiferromagnetic ordering to a ferromagnetic-like one in the previous study [26]. A similar single stepwise increase is observed for the $Ho_{79}Ce_{21}$ alloy, as illustrated in Fig. 11(a). This characteristic is more clearly evident in the H_{bias} dependence of χ', where a single peak is observed around the step field $\mu_0 H_{s1} \sim 0.4$ T, as shown in Fig. 11(b). Such responses to magnetic fields are typical of holmium-rich alloys (refer to *MH* curves in Ref. [23]).

In contrast, the $Ho_{48}Er_{47}Ce_5$ alloy exhibits steeper changes in M at two distinct nonzero magnetic fields, resulting in double peaks at $\mu_0 H_{c1} \sim 0.2$ T and $\mu_0 H_{c2} \sim 2$ T in the H_{bias} dependency. A similar double-step magnetization curve and double peaks in χ' (H_{bias}) are also observed for the $Ho_{25}Er_{75}$ alloy. The magnetic fields H_{c1} and H_{c2} correspond to H_m: the locations of scarps in the ΔS landscape. Given that multistep magnetization curves become more prevalent as the number of Er substitutions approaches or exceeds approximately half, it is plausible that these phenomena result from the interplay between the easy-plane magnetic anisotropy of Ho and the easy-axis magnetic anisotropy of Er. When competing magnetic forces are present, incommensurate antiferromagnetic structures, such as those observed here, frequently undergo successive phase transitions under an applied magnetic field. Although further research is necessary to clarify these transitions in detail, it can be concluded that the scarp structures

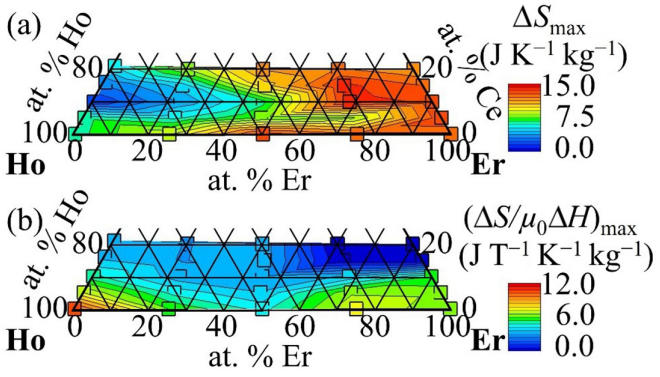

FIG. 12. Compositional dependence of (a) the maximum value of the total variation ΔS at $\mu_0 H = 5$ T (represented by the depth of the valley at locations indicated by ◊ in the ΔS landscape from Fig. 3), (b) maximum value of the variation rate $[(\Delta S/\Delta)(\mu_0 H)]$ (represented by the steepest slope in the ΔS landscape from Fig. 3).

in the ΔS landscapes arise from magnetic field-induced variations associated with antiferromagnetic components.

Conversely, the magnetization curves for the simple ferromagnets in the Ce-doped Er-rich alloy group are upwardly convex and free of anomalies. Consequently, their ΔS landscapes are notably straightforward.

F. Performance as magnetic refrigerants

Finally, we evaluated the magnetocaloric effects depicted in Fig. 3 from a practical perspective, incorporating our understanding of the magnetic structures. Recently, beyond the conventional cooling protocol that involves applying or removing a strong magnetic field of approximately 5 T, we introduced a highly efficient cooling protocol that employs a small oscillating magnetic field superimposed on a static magnetic field at the transition point [5]. For the conventional protocol, the total variation ΔS at $\mu_0 H = 5$ T serves as a crucial performance index. In contrast, the efficiency of this protocol should be assessed based on the rate of change, $\Delta S/\Delta(\mu_0 H)$.

Figure 12(a) illustrates the deepest valley depths in the landscape, corresponding to the total variation in ΔS from zero field to $\mu_0 H = 5$ T. For the Ce-doped Ho-rich alloy group, the deepest points are located in the high-temperature valleys within the paramagnetic phase. In contrast, for other alloys, the deepest points are associated with valleys corresponding to the onset of ferromagnetic components (indicated by open diamonds in Fig. 2). A general trend in Fig. 12(a) is that the valley depth $|\Delta S|$ increases with Er substitution for Ho, except in the Ce-doped Ho-rich alloy group. This compositional dependence aligns with the behavior of the ferromagnetic component at 5 K, as shown in Fig. 10(c). It is reasonable to expect that the magnitude of the magnetic field-induced entropy change correlates with the size of the ferromagnetic component, although a detailed analysis of this dependence is challenging. This difficulty arises because $|\Delta S|$ represents the cumulative entropy change from zero field to 5 T across a complex phase diagram, as previously discussed. The best performance in terms of $|\Delta S|$ is observed in the Ce-doped Er-rich alloy group. It is widely recognized that simple ferromagnetism tends to maximize the magnetocaloric effect at 5 T. The performance achieved, at $-14\,\mathrm{J}\cdot\mathrm{K}^{-1}\cdot\mathrm{Kg}^{-1}$, is not exceptionally superior to existing magnetic refrigerants such as $DyAl_2$, which achieves $-20\,\mathrm{J}\cdot\mathrm{K}^{-1}\cdot\mathrm{Kg}^{-1}$ [32]. However, ternary alloys with hexagonal structures are ductile, making them advantageous for specific applications. Before concluding, it is important to highlight the behavior of the Ce-doped Ho-rich alloy group. In this group, the valley depth on the paramagnetic side increases with higher Ce concentrations, despite a reduction in m_{eff}. The decrease in T_{c1} with Ce doping is more pronounced than the reductions in G and m_{eff}, as illustrated in Fig. 7. Assuming the magnetic couplings J_{AF} that form the antiferromagnetic structure are proportional to T_{c1}, and that $\Delta S(H)$ scales with $m_{\mathrm{eff}}H/J_{\mathrm{AF}}$ as predicted by a simple model [4], a larger $\Delta S(H)$ should occur at the same H for a system with smaller J_{AF}. This provides a plausible explanation for why ΔS (5 T) increases with Ce concentration in the Ce-doped Ho-rich alloy group.

Shifting focus to the variation rate $\Delta S/\Delta(\mu_0 H)$ at nonzero-bias magnetic field, the contour map in Fig. 12(b) illustrates the compositional dependence of $(\Delta S/\Delta(\mu_0 H))_{\mathrm{max}}$, the maximum magnitude of $\Delta S/\Delta(\mu_0 H)$. Data for the Ce-doped Er-rich alloy group are absent, as in simple ferromagnets the maximum variation typically occurs at zero magnetic field. Notably, $[(\Delta S/\Delta)(\mu_0 H)]_{\mathrm{max}}$ for all the ternary alloys is smaller than that for pure Ho metal. According to the Clausius-Clapeyron equation, the entropy change associated with a first-order phase transition is expressed as $\mu_0 \delta M \cdot (\partial H_m/\partial T)$, where δM is the change in magnetization caused by the transition at H_m. For Er-rich alloys, such as those in the $Ho_{50}Er_{50}$ and $Ho_{25}Er_{75}$ base alloy groups, the magnetization curves exhibit multistep structures. Consequently, the δM of each step is smaller than the single-step δM observed in pure Ho metal. This reduction in δM is a significant factor contributing to the decreased efficiency performance of $[(\Delta S/\Delta)(\mu_0 H)]_{\mathrm{max}}$ associated with erbium substitution.

On the other hand, as Ce concentration increases, m_{eff} decreases, as observed in Fig. 6(a). This study demonstrated that the magnetically ordered states at low temperatures remain largely consistent within the Ce-doped Ho-rich alloy group. Therefore, δM decreases alongside the reduction in total magnetization, as indicated by m_{eff} or $M_s/n\mu_0$ as shown in Fig. 6. For example, the magnitude of δM for $Ho_{79}Ce_{21}$ is smaller than that for pure Ho metal, as illustrated in Fig. 11(a). Furthermore, it is important to recall that magnetic clusters and inhomogeneities likely exist in this group of alloys, as discussed earlier. Figure 4(a) illustrates the field dependence of ΔS around the locations where the efficiency $[(\Delta S/\Delta)(\mu_0 H)]$ is maximized, with ΔS normalized by ΔS ($\mu_0 H = 5$ T). The data reveal that variations in $\Delta S/\Delta S$ ($\mu_0 H = 5$ T) with $\mu_0 H$ become more gradual around H_m as Ce concentration increases. In other words, the magnetic transition broadens with Ho substitution by Ce. This observation is consistent with the well-documented phenomenon where prior short-range orderings or inhomogeneities led to diffuse phase transitions in dilute systems [33]. As discussed, the broadening of the transition, along with the decrease in m_{eff}, contributes to the performance degradation of the single-step magnetization process in the Ce-doped Ho-rich alloy group.

V. SUMMARY AND PROSPECTIVE

Er- and Ce-substituted ternary alloys $Ho_{100-x-y}Er_xCe_y$ ($x < 100$, $y < 21$) were examined to further optimize magnetic refrigerants for the next generation of magnetic refrigeration technologies. The observed magnetic entropy changes in these alloys were complex, featuring twin valleys, various types of ridges, and the presence or absence of scarps in the ΔS landscapes across different concentration ranges. The origins of these features could not be conclusively determined through macroscopic measurements alone. To address this challenge, we developed a multisample neutron transmission spectroscopy technique and applied it to 25 different compositions of ternary alloys. The results allowed us to determine the overall change in spin structure correlated with the significant entropy changes. Specifically, the spectra revealed the presence of ferromagnetic components in all samples at lower temperatures, while the helical antiferromagnetic structures typical of pure heavy rare-earth metals were absent in the Ce-doped Er-rich alloy group. For the group exhibiting simple ferromagnetism, the magnetocaloric effect was notably enhanced at higher magnetic fields. Alloys with a simple hexagonal close-packed (hcp) structure, due to their enhanced ductility, proved more advantageous than intermetallic compounds, particularly when used as foil-shaped refrigerants in traditional magnetic refrigeration systems operating under high magnetic fields. Furthermore, heavy rare-earth alloys have been tested for their workability and durability in room-temperature magnetic refrigeration from Brown's seminal work [34] to recent prototypes [35], consistently meeting these stringent requirements. In this context, the discovery of a substantial magnetocaloric effect in ferromagnetic heavy rare-earth alloys is significant.

On the other hand, substituting Er with an uniaxial magnetic easy axis altered the metamagnetic transitions. Additionally, substituting with Ce, which strengthens the ferromagnetic interaction, rendered the ordered phase glassy and broadened the metamagnetic transition. Consequently, the rate of magnetic entropy change at these transitions decreased. This alloying approach did not directly improve the efficiency of the magnetic refrigeration protocol, which uses a small oscillating magnetic field superimposed on a static magnetic field. However, we can now select substitution elements that do not produce these effects from numerous candidates for future developments. In this context, the knowledge we have gained will be invaluable in guiding the design of future refrigerants for this refrigeration protocol.

The multisample neutron transmission spectroscopy method developed in this study proved particularly useful for roughly evaluating a large number of ternary alloy samples simultaneously. However, this method requires that all samples be measured at the same temperature and for the same duration, which limits the detailed analysis of individual samples. To address the remaining fundamental scientific issues, such as the origin of the inverse magnetic calorimetric effect observed in the $Ho_{50}Er_{50}$ base alloy group at extremely low magnetic fields and the relationship between the spin reorientation transition at low temperatures and the inverse magnetocaloric effects in the $Ho_{25}Er_{75}$ base alloy group, further research using neutron diffractometry is necessary. Neutron diffractometry can achieve higher precision and more easily optimize experimental conditions. In this context, the spectroscopy developed here serves as a broad, high-throughput complement to neutron-diffraction methods, which are precise but not well suited for screening large sample volumes. This method, along with scanning neutron diffractometry [36], facilitates the application of neutron analysis in industrial settings, including the discovery of materials and the screening of material compositions. The development of large data-driven materials research is emerging as a trend in the field of magnetic materials. Although advances in magnetic structure evaluation have not kept pace with other innovations, such as combinatorial synthesis and machine-learning based material design, this method holds promise as a significant advancement in bridging this gap.

ACKNOWLEDGMENTS

Experiments at BL22 of J-PARC were performed using user programs (Grants No. 2017A0042 and No. 2018A0062). A part of this work was supported by "Advanced Research Infrastructure for Materials and Nanotechnology in Japan(ARIM)" of the Ministry of Education, Culture, Sports, Science and Technology (MEXT) (Grant No. 24NM5119). This work was partially supported by JSPS KAKENHI (Grant No.19H04400) and JST-Mirai Program, Japan (Grant No. JPMJMI18A3).

H.M., K.H., and T.S. conducted the neutron imaging experiments; H.M. and N. Tsujii prepared the samples; H.M., N. Terada, and S.R.L. contributed significantly to the data analysis and interpretation; and T.O. supervised the study. All authors critically reviewed and revised the manuscript and approved the final version for submission.

[1] V. Franco, J. S. Blázquez, J. J. Ipus, J. Y. Law, L. M. Moreno-Ramírez, and A. Conde, Magnetocaloric effect: From materials research to refrigeration devices, Prog. Mater Sci. **93**, 112 (2018).

[2] H. Zhang, R. Gimaev, B. Kovalev, K. Kamilov, V. Zverev, and A. Tishin, Review on the materials and devices for magnetic refrigeration in the temperature range of nitrogen and hydrogen liquefaction, Phys. B: Condens. Matter **558**, 65 (2019).

[3] N. A. Zarkevich and V. I. Zverev, Viable materials with a giant magnetocaloric effect, Cryst. **10**, 815 (2020).

[4] R. Tamura, S. Tanaka, T. Ohno, and H. Kitazawa, Magnetic ordered structure dependence of magnetic refrigeration efficiency, J. Appl. Phys. **116**, 053908 (2014).

[5] N. Terada and H. Mamiya, High-efficiency magnetic refrigeration using holmium, Nat. Commun. **12**, 1212 (2021).

[6] A. Takeuchi and A. Inoue, Classification of bulk metallic glasses by atomic size difference, heat of mixing and period of constituent elements and its application to characterization of the main alloying element, Mater. Trans. **46**, 2817 (2005).

[7] R. Wang, Formation of metastable low temperature allotropic solid solutions in rare earth-zirconium systems, Metall. Trans. **3**, 1213 (1972).

[8] G. Shirane and S. J. Pickart, Neutron-diffraction studies of magnetic structures in Ho-Er alloys, J. Appl. Phys. **37**, 1032 (1966).

[9] R. A. Cowley, J. A. Simpson, C. Bryn-Jacobsen, R. C. C. Ward, M. R. Wells, and D. F. McMorrow, Magnetic phase diagram of Ho/Er alloys, Phys. Rev. B **57**, 8394 (1998).

[10] L. A. Ugodnikova, S. G. Chuchman, and L. M. Noskova, Magnetic states diagram of alloys of heavy rare-earth metals with scandium, yttrium, lanthanium and lutetium, Phys. Met. Metall. **52**, 163 (1981).

[11] S. Kawano and N. Achiwa, Magnetic structure of hcp Ho/Ce and Er/Ce alloys, Physica B+C **120**, 220 (1983).

[12] D. Hughes, M. Däne, A. Ernst, W. Hergert, M. Läders, J. Poulter, J. B. Staunton, A. Svane, Z. Szotek, and W. M. Temmerman, Lanthanide contraction and magnetism in the heavy rare earth elements, Nature (London) **446**, 650 (2007).

[13] E. Mendive-Tapia and J. B. Staunton, Theory of magnetic ordering in the heavy rare earths: Ab initio electronic origin of pair- and four-spin interactions, Phys. Rev. Lett. **118**, 197202 (2017).

[14] F. Salvemini, V. Luzin, M. Avdeev, A. Tremsin, A. Sokolova, A. Gregg, C. Wensrich, S. Gatenby, M. J. Kim, and F. Grazzi, Samurai's swords, a non-invasive investigation by neutron techniques, Mater. Sci. Forum **983**, 15 (2020).

[15] Y. Su, K. Oikawa, T. Shinohara, T. Kai, T. Horino, O. Idohara, Y. Misaka, and Y. Tomota, Neutron Bragg-edge transmission imaging for microstructure and residual strain in induction hardened gears, Sci. Rep. **11**, 4155 (2021).

[16] D. K. Aswal, P. S. Sarkar, and Y. S. Kashyap, *Neutron Imaging Basics, Techniques and Applications* (Springer, Singapore, 2022).

[17] H. Mamiya, Y. Oba, N. Terada, N. Watanabe, K. Hiroi, T. Shinohara, and K. Oikawa, Magnetic Bragg dip and Bragg edge in neutron transmission spectra of typical spin superstructures, Sci. Rep. **7**, 15516 (2017).

[18] H. Mamiya, Y. Oba, N. Terada, K. Hiroi, T. Ohkubo, and T. Shinohara, Neutron imaging for magnetization inside an operating inductor, Sci. Rep. **13**, 9184 (2023).

[19] G. L. Squires, *Introduction to the Theory of Thermal Neutron Scattering* (Cambridge University Press, New York, 2012).

[20] H. Sato, Deriving quantitative crystallographic information from the wavelength-resolved neutron transmission analysis performed in imaging mode, J. Imaging **4**, 7 (2018).

[21] M. Kataoka, Ferromagnetic system with the first order transition and applicability of the Maxwell relation to its magnetocaloric effect, J. Magn. Magn. Mater. **469**, 494 (2019).

[22] T. Shinohara, T. Kai, K. Oikawa, T. Nakatani, M. Segawa, K. Hiroi, Y. Su, M. Ooi, M. Harada, H. Iikura, H. Hayashida, J. D. Parker, Y. Matsumoto, T. Kamiyama, H. Sato, and Y. Kiyanagi, The energy-resolved neutron imaging system, RADEN, Rev. Sci. Instrum. **91**, 043302 (2020).

[23] See Supplemental Material at http://link.aps.org/supplemental/10.1103/PhysRevResearch.7.013233 for detailed XRD, magnetic, magnetocaloric, and neutron spectroscopy data for all samples, including the typical examples described in the main text.

[24] I. R. Harris and J. D. Speight, Lattice spacing variations in some intra-rare-earth alloy systems, J. Less-Common Met. **114**, 183 (1985).

[25] M. Norman, I. R. Harris, and G. V. Raynor, Lattice spacings and effective atomic diameters in the ternary systems formed by Th and Ce with Y, La, Gd, and Er, and by Th, Pr and Y, J. Less-Common Met. **13**, 24 (1967).

[26] R. J. Elliott, *Magnetic Properties of Rare Earth Metals* (Springer, New York, 1972).

[27] A. P. Young, *Spin Glasses and Random Fields* (World Scientific, Singapore, 1997).

[28] E. P. Wohlfarth and K. H. J. Buschow, *Handbook of Ferromagnetic Materials* (Elsevier, Amsterdam, 1988), Vol. 4.

[29] K. H. Fischer and J. A. Hertz, *Spin Glasses* (Cambridge University Press, New York, 1991).

[30] T. Paakkari, A determination of the Debye–Waller temperature factor and the X-ray Debye temperature for Ni, Cr, Fe, Mo, and W, Acta Crystallogr. **A30**, 83 (1974).

[31] S. Kawano and N. Achiwa, Annual report research reactor institute, Kyoto University **19**, 23 (1986).

[32] T. Hashimoto, T. Kuzuhara, M. Sahashi, K. Inomata, A. Tomokiyo, and H. Yayama, New application of complex magnetic materials to the magnetic refrigerant in an Ericsson magnetic refrigerator, J. Appl. Phys. **62**, 3873 (1987).

[33] K. Takeda, Drastic reduction of TN in a quasi-one-dimensional Ising spin system with small amount of impurity spin, J. Phys. Soc. Jpn. **40**, 1781 (1976).

[34] G. V. Brown, Magnetic heat pumping near room temperature, J. Appl. Phys. **47**, 3673 (1976).

[35] S. Lionte, M. Risser, and C. Muller, A 15 kW magnetocaloric proof-of-concept unit: Initial development and first experimental results, Inter. J. Refrig. **122**, 256 (2021).

[36] K. Ohoyama, K. Isawa, and K. Yamada, Scanning wide-angle neutron diffraction and its application to local structures investigations in stainless steel, Jpn. J. Appl. Phys. **46**, 7925 (2007).